Ignored role of polyphenol in boosting reactive oxygen species generation for polyphenol/chemodynamic combination therapy

Huijia Mao [a],[1], Yangyang Wen [b],[1], Yonghui Yu [a], Hongyan Li [a],[*], Jing Wang [a],[**], Baoguo Sun [a]

[a] China-Canada Joint Lab of Food Nutrition and Health (Beijing), School of Food and Health, Beijing Technology and Business University (BTBU), 11 Fucheng Road, Beijing, 100048, China
[b] College of Chemistry and Materials Engineering, Beijing Technology and Business University (BTBU), 11 Fucheng Road, Beijing, 100048, China

ARTICLE INFO

ABSTRACT

Chemodynamic therapy (CDT) is a promising tumor-specific treatment, but still suffering insufficient reactive oxygen species (ROS) levels due to its limited efficacy of Fenton/Fenton-like reaction. Polyphenol, as a natural reductant, has been applied to promote the efficacy of Fenton/Fenton-like reactions; however, its intrinsic pro-apoptosis effects was ignored. Herein, a novel CDT/polyphenol-combined strategy was designed, based on Avenanthramide C-loaded dendritic mesoporous silica (DMSN)-Au/Fe$_3$O$_4$ nanoplatforms with folic acid modification for tumor-site targeting. For the first time, we showed that the nanocomplex (DMSNAF-AVC-FA) induced ROS production in the cytoplasm via Au/Fe$_3$O$_4$-mediated Fenton reactions and externally damaged the mitochondrial membrane; simultaneously, the resultant increased mitochondrial membrane permeability can facilitate the migration of AVC into mitochondrial, targeting the DDX3 pathway and impairing the electron transport chain (ETC) complexes, which significantly boosted the endogenous ROS levels inside the mitochondrial. Under the elevated oxidative stress level via both intra- and extra-mitochondrial ROS production, the maximum mitochondrial membrane permeability was achieved by up-regulation of Bax/Bcl-2, and thereby led to massive release of Cytochrome C and maximum tumor cell apoptosis via Caspase-3 pathway. As a result, the as-designed strategy achieved synergistic cytotoxicity to 4T1 tumor cells with the cell apoptosis rate of 99.12% *in vitro* and the tumor growth inhibition rate of 63.3% *in vivo*, while very minor cytotoxicity to normal cells with cell viability of 95.4%. This work evidenced that natural bioactive compounds are powerful for synergistically boosting ROS level, providing new insight for accelerating the clinical conversion progress of CDT with minimal side effects.

1. Introduction

Reactive oxygen species (ROS) are a group of highly reactive ions or free radicals, including singlet oxygen (^{1}O$_2$), hydroxyl radicals (•OH), superoxide anions (O$_2$•$^-$), and peroxides (O$_2^{2-}$) [1,2]. In malignant tumor cells, excessive ROS can be utilized to trigger oxidative stress, leading to DNA damage [3], protein inactivation [4], phospholipid membrane peroxidation, and final cell apoptosis [5]. In this case, chemodynamic therapy (CDT), utilizing Fenton/Fenton-like reactions triggered by the tumor microenvironment (TME) for promoting ROS accumulation, has been recently developed and become a popular research focus for cancer treatment [6–9]. However, the CDT performance is highly dependent on TME conditions, for example, the limited level of endogenous H$_2$O$_2$, the

weak acidity (pH~6.5), and high content of reducing substances (e.g., glutathione, GSH) are not favorable for most of Fenton/Fenton-like catalytic reactions, and thereby reducing the therapeutic efficacy of CDT [10]. Therefore, development of the combined therapy strategy for a boosted ROS generation is encouraged to overcome the relatively low therapeutic effect of single CDT treatment [11,12]. The combination of chemotherapeutic drugs and CDT is a promising strategy to achieve improved anticancer effects [13]. Some chemotherapeutic drugs, e.g., cisplatin, doxorubincin, arsenic trioxide, and etoposide, have been applied in clinical practice and mediated the antitumor effect by the generation of H$_2$O$_2$ [14–16]. For instance, Xue et al. successfully prepared a combined CDT-chemotherapy nanoplatform against cancer by loading doxorubicin (DOX) and modified hyaluronic acid (HA) on a

---

* Corresponding author.
** Corresponding author.
E-mail addresses: hongyan.li@btbu.edu.cn (H. Li), wangjing@th.btbu.edu.cn (J. Wang).
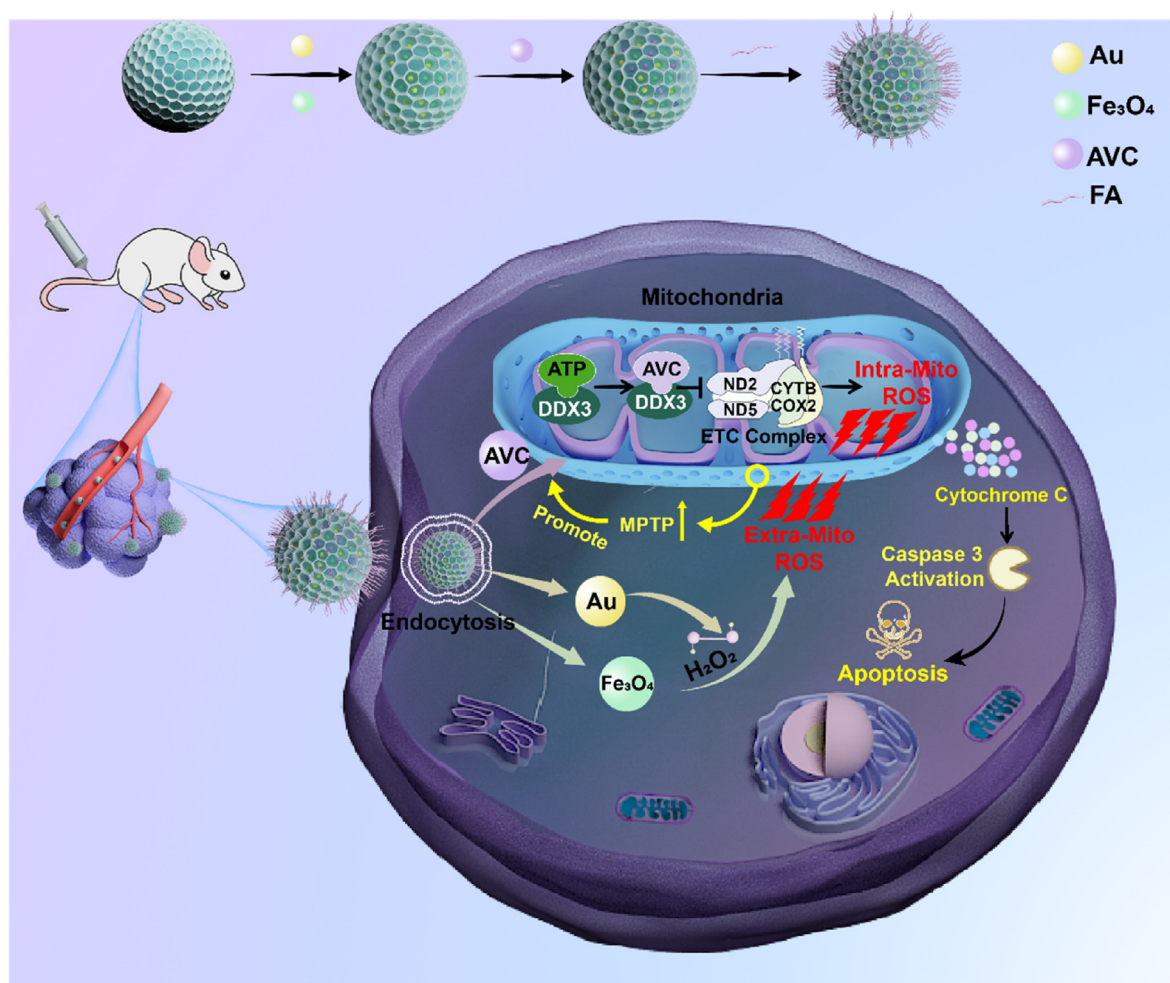[1] These authors contributed equally to this study.

Fig. 1. Schematic representation of the synthesis of DMSNAF-AVC-FA nanoparticles and the use of DMSNAF- AVC-FA to induce intensive CDT therapy.

metal-organic framework (MOF) material, MIL-100. The obtained MIL-100@DOX-HA nanoparticles (NPs), acting as drug nanocarrier with high DOX loading efficiency for chemotherapy, produced a large amount of toxic ROS for the CDT treatment and synergistically improved antitumor efficacy [17]. Xu et al. constructed a multifunctional nanoplatform based on DOX-loaded tannic acid-iron network for combined chemo-/-chemodynamic therapy, caused significant immunogenic cell death via cooperative Fe-based CDT and DOX chemotherapy [18]. Ding et al. reported a facile and versatile method for the *in situ* growth of MnO_2 directly on the surface of up-conversion nanoparticles as ideal TME-responsive nanoplatforms (UCMn) to anchor the cisplatin prodrug and achieve high-efficiency synergistic CDT-chemotherapy of tumors [19]. Yet, this combined strategy are still challenged by various factors, such as the large toxic side effects, the low loading stability, and burst drug release [20].

Polyphenols, the secondary metabolites from dietary fruit and vegetables, are well-known as natural antioxidants, are conventionally regarded as chemopreventive agent at the forefront of oncological research [21,22]. Recently, the pro-apoptosis effect of polyphenol has been identified and applied in clinical tumor treatments [23]. Polyphenols can mediate ROS generation via mitochondrial intrinsic apoptotic, thus inducing apoptosis of malignant cells. To be specific, some natural compounds (e.g., quercetin [24], apigenin [25], alkaloids [21]) activate the formation of ROS that disrupts the mitochondrial membrane and interferes with mitochondrial electron transfer chain, resulting in the release of Cytochrome C. In the cytosol, the binding of cytochrome C to apoptotic protease activates factor 1 in the presence of

ATP/dATP, which induces activation of Caspase-9 and Caspase-3 successively, and finally leads to the apoptotic cell death [23]. In addition to the pro-apoptosis, the most major advantage of polyphenol as therapeutic strategy is the redox differences between cancer and normal cells that contributes to the selective cytotoxicity of polyphenols targeting tumor cells [23,26–28]. Fu et al. explored the anti-carcinogenic mechanism of avenanthramides (AVNs) that are antioxidants exclusively present in oats, and found that the high ROS level in cancer cells facilitated AVNs to target dead-box RNA helicase 3 (DDX3), consequently triggering further excessive production of ROS [29]. To date, to the best of our knowledge, there are few studies that applied polyphenol into CDT based combination treatments [30]. In the reported studies, polyphenols are mostly used for formation of metal-phenolic network as drug carriers for either maximizing drug loading due to the superior biocompatibility, acidic sensitivity, and feasible modifications [31,32] or promoting the efficacy of Fenton/Fenton-like reaction by accelerating the conversion between Fe^{3+} and Fe^{2+}. However, the intrinsic antitumor function of polyphenol is always ignored.

Inspired by the pro-oxidant effects of natural polyphenols, especially the mediation of intracellular ROS generation via electron transport chain (ETC) complex, the combination of natural polyphenol and CDT strategy was firstly designed to strengthen intracellular ROS production for a promoted antitumor performance. Herein, avenanthramide C (AVC), a unique natural polyphenol presenting in oats, was selected as pro-oxidant agent to construct the intelligent nanocatalytic theranostics. As shown in Fig. 1, the *in situ* deposition of Au and Fe_3O_4 was firstly loaded to dendritic mesoporous silica nanoparticles (DMSN), endowing

this nanoplatform (DMSNAF) with CDT functionality. Then, AVC was decorated on the DMSNAF to facilitate ROS generation. Lastly, biocompatible folic acid (FA) was anchored onto the surface of platform to promote targeting efficacy (ADSNAF-AVC-FA NPs). After being internalized by tumor cells, i) Au and Fe_3O_4 NPs with glucose oxidase and peroxidase-like activity, respectively, performed ROS-mediated cascade reactions to guarantee a high ROS level in tumor cell cytoplasm. ii) The high extra-mitochondrial ROS increased the mitochondrial membrane permeability, as indicated by the upregulation of protein level of Bax/Bcl-2. iii) Meanwhile, the increased mitochondrial membrane permeability facilitated migration of AVC into mitochondrial to target the DDX3 pathway and to impair the ETC complexes, which further boosted the endogenous ROS levels inside the mitochondrial. iv) Under the elevated oxidative stress level via both intra- and extra-mitochondrial ROS production, ADSNAF-AVC-FA displayed significantly synergistic antitumor efficacy, as well as excellent biocompatibility, biosafety, and selective cytotoxicity. This combined therapy not only complements the importance of polyphenol in assisting CDT for maximum antitumor efficacy, but also provides new insights for accelerating the clinical conversion progress of CDT with minimal side effects.

2. Materials and methods

2.1. Materials

Sodium salicylate (NaSal), triethanolamine (TEA), Tetraethyl orthosilicate (TEOS), cetyltrimethylammonium bromide (CTAB), (3-Aminopropyl) triethoxysilane, iron chloride ($FeCl_3·6H_2O$), oleyl alcohol, sodium oleate, $HAuCl_4·4H_2O$, diphenyl ether, sodium phosphate dibasic (Na_2HPO_4), and acetic acid were obtained from Macklin Biochemical Co, Ltd (Shanghai, Chain). Acetone, *n*-hexane and ethanol were purchased from Fuchen Chemical Reagent Co, Ltd (Tianjin, China). 3,3′,5,5′-tetramethylbenzidine (TMB) was obtained from Aladdin Co, Ltd (Shanghai, China). Hydrochloric acid (HCl), glucose, and H_2O_2 were ordered from Sinopharm Chemical Reagent Co, Ltd (Shanghai, China). Fluorescein isothiocyanate (FITC) and Methoxy PEG-thiol (mPEG-SH, Mw = 5000) were obtained from xi'an ruixi Biological Technology Co, Ltd (xi'an, Chain). Dimethyl sulfoxide (DMSO) was from Merck Co. Inc. (Germany).

2.2. Synthesis of DMSN, DMSNAF

DMSN, DMSNAF were synthesized by a method of Gao et al. with a slight modification [33].

2.3. Drug loading and release

The solutions of DMSN or DMSNAF were prepared by dispersion in DMSO (1 mg mL^{-1}). AVC was dissolved in 50% DMSO aqueous solution, and homogeneously mixed with DMSN or DMSNAF solutions, and then incubated at 37 °C for 24 h. After the mixtures were centrifuged under 10,000 rpm, the precipitations were washed with ethanol three times to remove the free AVC. The supernatant and washing solution were also collected to measure the amount of AVC contained nanoparticles by a UV–vis spectrophotometer. Drug loading efficiency and loading capacity were calculated by Formulas (1-2):

$$\text{Loading efficiency} = 100\% \times (\text{m}_{\text{total AVC}} - \text{m}_{\text{unloaded AVC}}) \ / \ \text{m}_{\text{total AVC}} \quad (1)$$

$$\text{Loading capacity} = 100\% \times (\text{m}_{\text{total AVC}} - \text{m}_{\text{unloaded AVC}}) \ / \ \text{m}_{\text{total DMSN}} \quad (2)$$

To study the drug release, AVC-loaded DMSN or DMSNAF were dispersed in PBS solution (pH = 6.5). After incubation at 37 °C for different times, the samples were centrifuged at 10,000 rpm (4 °C) and the supernatant was carefully collected and determined the amount of released AVC using UV–vis.

To improve the biocompatibility of nanoparticles, DMSNAF-AVC was treated by PEGylation. 25 mg NHS-mPEG-FA was added into the DMSNAF-AVC anhydrous ethanol solution (20 mL, 1.5 mg mL^{-1}), and stirred for 12 h at room temperature. After centrifugation and washing with water, the PEGylated DMSNAF-AVC-FA NPs were obtained.

2.4. Amine group quantification

The amount of amine group represents the active sites for PEG modification. Briefly, 100 μg DMSNAF-AVC and DMSNAF-AVC-FA were dispersed into 100 μL of DI water, respectively. Then, 100 μL of ninhydrin solution (2 w/v%) was mixed for chromogenic reaction at 90 °C for 20 min. After the mixtures were cooled down to room temperature, 800 μL of ethanol was added to stop the reaction, and the absorbance at 570 nm using a microplate reader was recorded. Glycine solutions from 5 to 25 mM were used to plot a standard curve [34].

2.5. Catalytic activity measurements of DMSNAF-AVC NPs

Glucose, instead of H_2O_2, was used to further evaluate the self-organized enzymatic cascade reaction of the DMSNAF NPs (pH = 6.5, 7.4). The DMSNAF-AVC-FA NPs, glucose and TMB were incubated for 1 h. The absorbance at 370 nm and 650 nm were detected.

2.6. Study of •OH generation

In the ESR experiment, DMSN, DMSN-AVC, DMSNAF and DMSNAF-AVC-FA (200 μg/mL) was placed in acidic phosphoric buffer solution (pH 6.5) containing glucose (10 mM). After stirring for 1 h, 5,5-dimethyl-pyrroline *N*-oxide (DMPO) was added to the solution and tested immediately.

Cell Culture: 4TI cells, L6 cells, and H1299 cells (purchased from ATCC) were cultured in dulbecco's modified eagle's medium (DMEM, high glucose, Gibco, USA) with 10% fetal bovine serum (FBS, Gibco, USA), and 1% penicillin/streptomycin (Gibco, USA) at 37 °C.

2.7. Western blot assay

4T1 cells were incubated in 6-well plates. After the indicated treatments, cells were washed three times with ice-cold PBS, followed by the addition of RIPA lysis buffer (Solarbio, R0010, China) supplemented with protease and phosphatase inhibitor PMSF. Lysates were cleared by centrifugation at 12,000 g for 10 min at 4 °C, and BCA Protein Assay Kit (Solarbio, PC0020, China) was employed to determine the protein concentrations. After being heated with loading buffer, equal amounts of total proteins were separated on 10% or 12% SDS-polyacrylamide gel electrophoresis gels and transferred to a polyvinylidene difluoride (PVDF) membranes. After blocking with tris-buffered saline with Tween 20 (TBST) containing 5% skim milk for 1 h, the membranes

incubated with various primary antibodies against Cytochrome C (ABclonal, A4912), Bcl-2 (ABclonal, A19693), Bax (ABclonal, A19684), Caspase 3 (ABclonal, A2156), GPX4 (ABclonal, A11243) ND2 (ABclonal, A17968), ND5, (ABclonal, A17972), COX2 (ABclonal, A1253), MY-CYB (ABclonal, A17966), TIM23 (ABclonal, A8688), DDX3 (ABclonal, A5637) and β-actin (ABclonal, AC038) at 4 °C overnight. After that, PVDF membranes were washed with TBST for 3 times and incubated with horseradish peroxidase (HRP)-labeled goat anti-rabbit IgG H + L) secondary antibody (ABclonal, AS014) for 2 h. Followed by the addition of ECL Basic Kit (ABclonal, RM00020) to react for 2 min, and the signals were recorded on a Bio-Rad ChemiDoc MP System (Bio-Rad Laboratories, USA).

2.8. Cell viability assay

The cytoprotective activity of nanoparticles was investigated by MTT assay in 4T1 cells. The 10^5 4T1 cells/mL were grown in 96-well microplates. After 24 h incubation, cells were treated with various
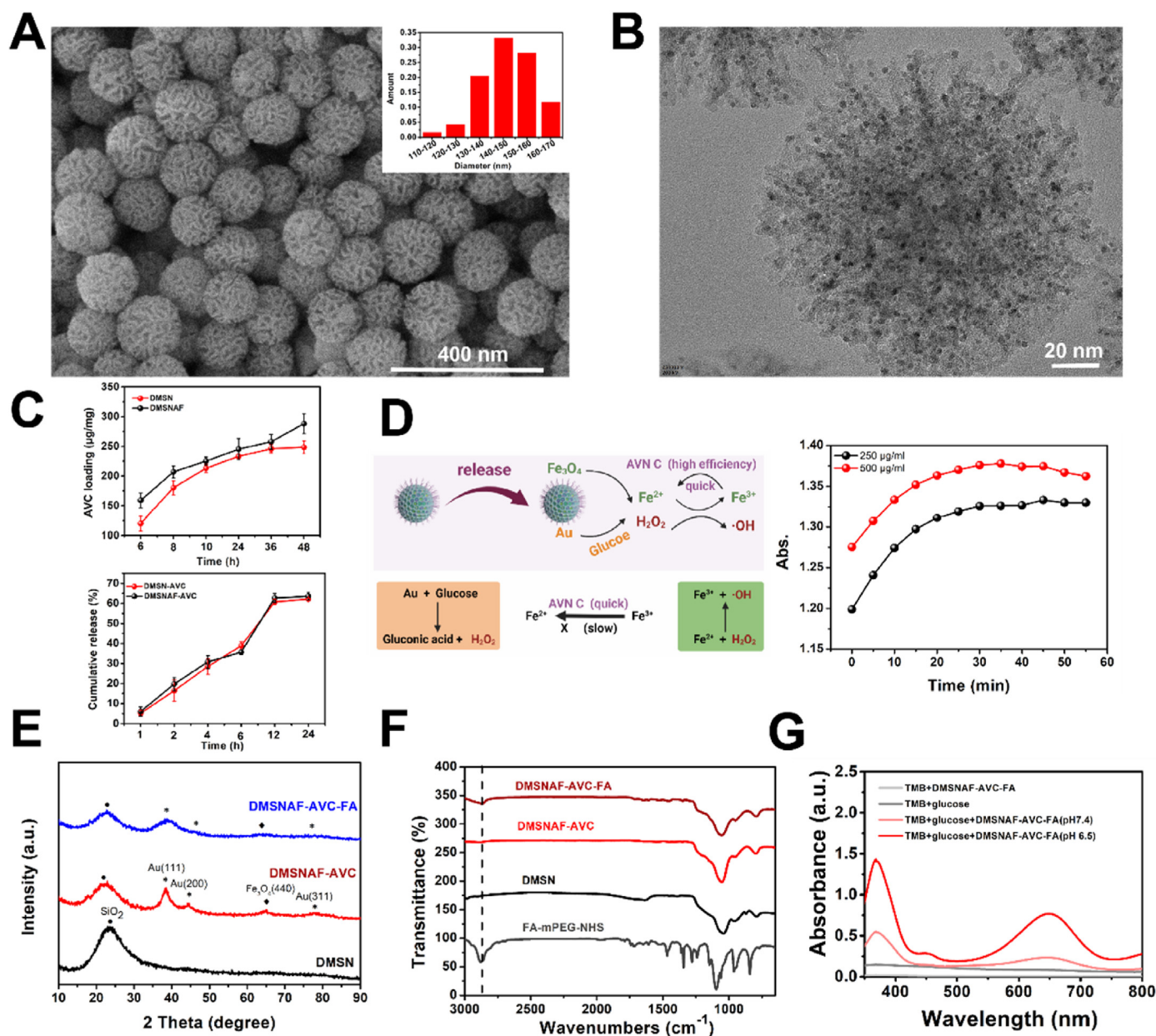
Fig. 2. (A) Typical SEM and (B) TEM images of DMSNAF-AVC. (C) AVC loading capacities of DMSN and DMSNAF NPs (above); AVC release property of DMSN-AVC and DMSNAF-AVC in PBS solution (1 mg mL^{-1}, pH 6.5, below). (D) Illustration of the mechanism of self-supplied H_2O_2 and acceleration of Fe (III)/Fe (II) conversion by AVC (left). AVC reduced Fe (III) into Fe (II) due to its reductive ability (right). (E) XRD patterns of DMSN, DMSNAF-AVC and DMSNAF-AVC-FA NPs. (F) FTIR spectra of FA-mPEG-NHS, DMSN, DMSNAF-AVC and DMSNAF-AVC-FA samples. (G) UV–vis absorption spectra of the catalyzed oxidation of TMB (oxTMB) in the presence of DMSNAF-AVC-FA nanocatalyst.

concentrations of AVC (30, 60, 90 μg mL^{-1}) along with H_2O_2 (0.1–0.4 mM). Similarly, cells without AVC + H_2O_2 and only treated with H_2O_2 were considered as positive and negative controls, respectively. The viability of cells was evaluated by MTT assay by measuring absorbance at 450 nm. *Live and dead cells observation*: 4T1 cells were incubated in 6-well plates. After 24 h, the culture medium was replaced with fresh ones containing different NPs. 12 h later, all groups were stained by calcein-AM and PI for further alive/dead observation.

2.9. Flow cytometry

4T1 cells were incubated in 6-well plates for 24 h. After different treatments, cells were trypsinized and washed. Subsequently, cells were resuspended in 0.5 mL of binding solution, followed by addition of annexin V-FITC and PI. After 15 min of incubation at room temperature,

cells were rinsed with PBS and analyzed immediately using a flow cytometer. Cells treated with pure culture medium was set as control.

Cell Endocytosis Test: 4T1 cells were plated in 15-mm cell culture dishes (NEST, 801,002) with an initial density of 2×10^5 cells/dish. After 12 h of incubation, cells were treated with FITC-labeled DMSNAF-AVC dispersed in culture medium. After coincubation durations 2 h, 4',6-diamidino-2-phenylindole (DAPI, Beyotime, C1002) was added into each dish and used to stain nuclei under dark for 15 min. Subsequently, the cells were washed with PBS for three times gently and observed under FV 3000 RS confocal fluorescence microscope (CLSM) (Olympus Company, Japan).

2.10. Intracellular ROS detection

Cells were seeded in 6-well plates. After 12 h of incubation, cells were

treated with different NPs dispersed in culture medium for 8 h. Cells treated with pure culture medium was set as control. Then, the culture mediums were discarded followed by PBS rinsing for three times, and the fresh culture medium containing DCFH-DA (Beyotime, S0033) was added into each dish and used for staining under dark for 15 min. Subsequently, the cells were washed with PBS for the other three times gently and observed under FV3000RS CLSM.

2.11. Animals and tumor model

All animal experiment procedures were confirmed to the guidelines of the Animal Care Ethics Commission of Charles river (ID: P2021086). 4-week-old female Balb/c mice were purchased from Vital River Laboratories. To establish xenografted tumors, 4T1 cells were harvested and suspended in the PBS at a density of 2×10^7 cells mL^{-1}. Then 100 μL cell suspension was injected subcutaneously into the right flank of mice. The length and width of breast tumor xenografts were measured every 2 days and the tumor volumes were calculated according to the following formula: volume = length × (width)^2/2.

2.12. In vivo fluorescent imaging and biodistribution

Cy7 fluorescent dye was introduced to tag DMSNAF-AVC NPs for *in vivo* fluorescence imaging. The synthesis steps strictly followed the previous procedure. After intravenous injection, the 4T1 breast cancer-bearing mice were imaged under an IVIS system with an excitation wavelength of 700 nm and an emission wavelength of 790 nm at different time intervals (2, 4, 8, 12, and 24 h). After 24 h, the mice were sacrificed, The major organs (lungs, kidneys, hearts, spleens, and livers) and tumor tissues were excised and imaged ex vivo with the same excitation (700 nm) and emission (790 nm).

2.13. In vivo therapeutic efficacy

Once tumors reached ~50 mm^3, the 4T1 subcutaneous tumor-bearing mice were divided into 6 groups for different treatments as follows: 1) PBS, 2) DMSN, 3) DMSN-AVC, 4) DMSN-DOX, 5) DMSNAF, 6) DOX-DMSNAF, 7) DMSNAF-AVC-FA (100 μL saline solution, dose 10 mg kg^{-1}) [33,35–38]. All mice received four times of intravenous injections with different agents at day 1, 4, 7 and 10. Tumor size and body weights were measured every 2 days. After 14 days post-treatment, all the mice were sacrificed, and the tumors were excised and weighted. The tumor growth inhibition index (TGI) on day 14 was calculated in accordance with formula:

$$TGI = (V_C - V_T) \ / \ V_C \times 100\%$$

where V_C and V_T represented the tumor volume of saline and a certain treatment group, respectively.

2.14. Histology and immunofluorescence staining

After the treatment, the mice were sacrificed and major organs (lungs, kidneys, hearts, spleens, and livers) and tumor tissues were collected and fixed in 4% paraformaldehyde. The fixed tumor tissues were sliced and stained with H&E, terminal deoxynucleotidyl transferase dUTP nick end labeling (TUNEL) according to the instructions. he major organs (lungs, kidneys, hearts, spleens, and livers) were sectioned and stained with H&E, followed by the observation under optical microscopy to confirm the biocompatibility of treated materials.

2.15. Hemolysis test

Fresh mouse red blood cells (RBC) (2 mL) were added to 20 mL of normal saline (NS) and preheated at 37 °C to prepare the blood diluent. Next, 100 μL of the mouse blood diluent was added to a 2 mL Eppendorf tube, followed by addition of 900 μL of H$_2$O as a positive control, 900 μL of normal saline as a negative control, and 900 μL of DMSNAF-AVC NPs at different concentrations. The samples were incubated in a water bath at 37 °C for 2 h and centrifuged at 3000 rpm for 3 min. The supernatant was collected and used for UV measurement at 540 nm absorbance.

2.16. Statistical analysis

All the data were presented as mean ± standard deviation (s.d.). Statistical significance was calculated via one-way ANOVA with a Tukey post-hoc test and $p < 0.05$ was considered statistically significant.

3. Results and discussion

3.1. Preparation and characterization of DMSNAF-AVC-FA NPs

The preparation steps of DMSNAF-AVC-FA NPs were illustrated in Fig. 1. The DMSN with unique dendritic mesopores and splendid biocompatibility were chosen as nanocarriers for the loading of Au, Fe$_3$O$_4$ and AVC through *in situ* encapsulation. To investigate the roles of nanozyme NPs and AVC, we synthesized pristine DMSN, AVC-free nanoparticles, nanozyme-free nanoparticles, nanozymes- and AVC-coloaded nanoparticles, ascribed as DMSN, DMSNAF, DMSN-AVC and DMSNAF-AVC, respectively. Scanning electron microscope (SEM) images showed that nanozyme and AVC loadings did not affect the morphology of DMSN (Fig. 2A and Supplementary Fig. S1), with an average particle size of ~140 nm for DMSNAF-AVC. Transmission electron microscopy (TEM) image disclosed that Au and Fe$_3$O$_4$ NPs were ultrasmall particles with well-confined size uniformity (Supplementary Fig. S2), and evenly decorated within the mesopores of DMSN matrix (Fig. 2B). Furthermore, dark-field TEM image and elemental mappings showed a homogeneous distribution of Si, O, Au, and Fe in DMSNAF-AVC, confirming the successful synthesis of uniform nanocomposites (Supplementary Fig. S3). As demonstrated in Fig. 2C, both DMSN and DMSNAF have high AVC loading rates, with 248.37 μg mg^{-1} and 288.06 μg mg^{-1}, respectively. The slightly increased value of DMSNAF is mainly attributed to the rough surface inside of the mesopores, which was also verified by the increased surface area from pristine DMSN to DMSNAF (325.9 m^2 g^{-1} and 523.5 m^2 g^{-1}, respectively, Supplementary Fig. S4). In addition, DMSNAF-AVC showed a quick drug releasing behavior, with a AVC release rate of reaching 62% at 12 h (Fig. 2C), and it was mainly associated with its unobstructed dendritic mesopores. As a nanocatalyst, the AVC in DMSNAF-AVC produced an imperative effect on the conversion of Fe^{3+} (low catalytic efficiency) into Fe^{2+} (high catalytic efficiency), resulting in a significantly boosted Fenton reaction efficiency (as illustrated in Fig. 2D, left). As it was evidenced, the concentration of Fe^{2+} slightly increased with the prolonged time in the solutions of AVC and Fe^{3+}, and as Fe^{3+} dosage elevated, Fe^{2+} level reached its maximum within a very short time (only 30 min, Fig. 2D, right).

To enhance the cancer cell-targeting functionality and final tumor accumulation of nanodrugs, DMSNAF-AVC NPs were further modified with folic acid using NHS-PEG-FA, named as DMSNAF-AVC-FA. The final particle size of DMSNAF-AVC-FA was 150 nm (Supplementary Fig. S5), with a surface zeta potential of −1.56 mV (Supplementary Fig. S6). While the X-ray diffraction (XRD) analysis showed that the loadings of AVC and FA did not change the crystallinity of Au and Fe$_3$O$_4$ NPs (Fig. 2E). The decrease amount of amino group represents the modification amount of the folic acid molecule. It can be calculated from Supplementary Table S1 that 65% of the amine groups of DMSNAF-AVC reacted with FA-mPEG-NHS. Simultaneously, FT-IR spectra identified the FA coating on the nanocatalyst (Fig. 2F), confirming the successful synthesis of DMSNAF-AVC-FA product. In addition, after soaking DMSNAF-AVC-FA in water, phosphate-buffered saline (PBS), and cell medium for 24 h, the solution was still uniform and translucent. This indicated good dispersion and stability of DMSNAF-AVC-FA in the stock solution probably due to the presence of mPEG (Supplementary Fig. S7). As illustrated in Fig. 1, the
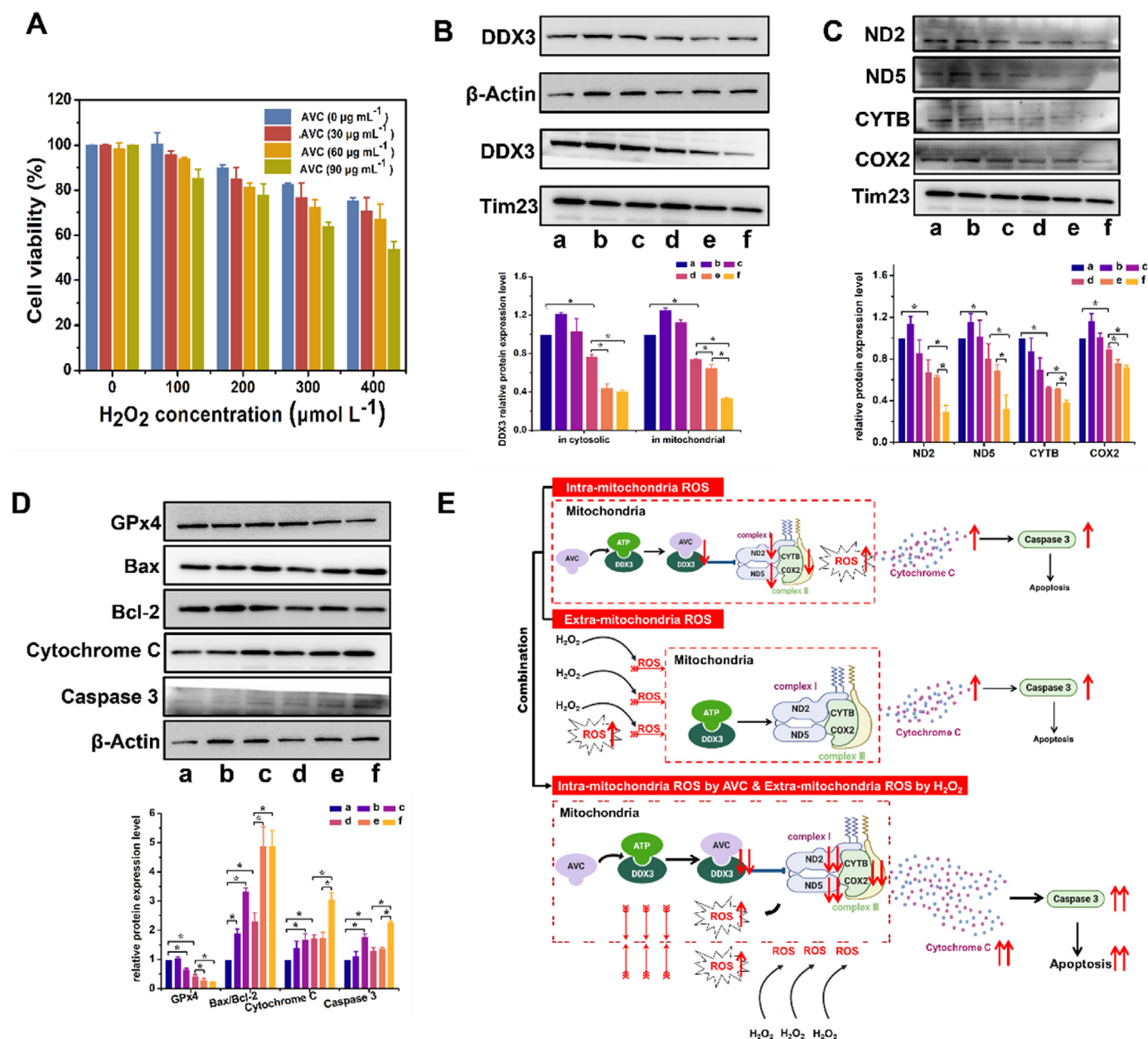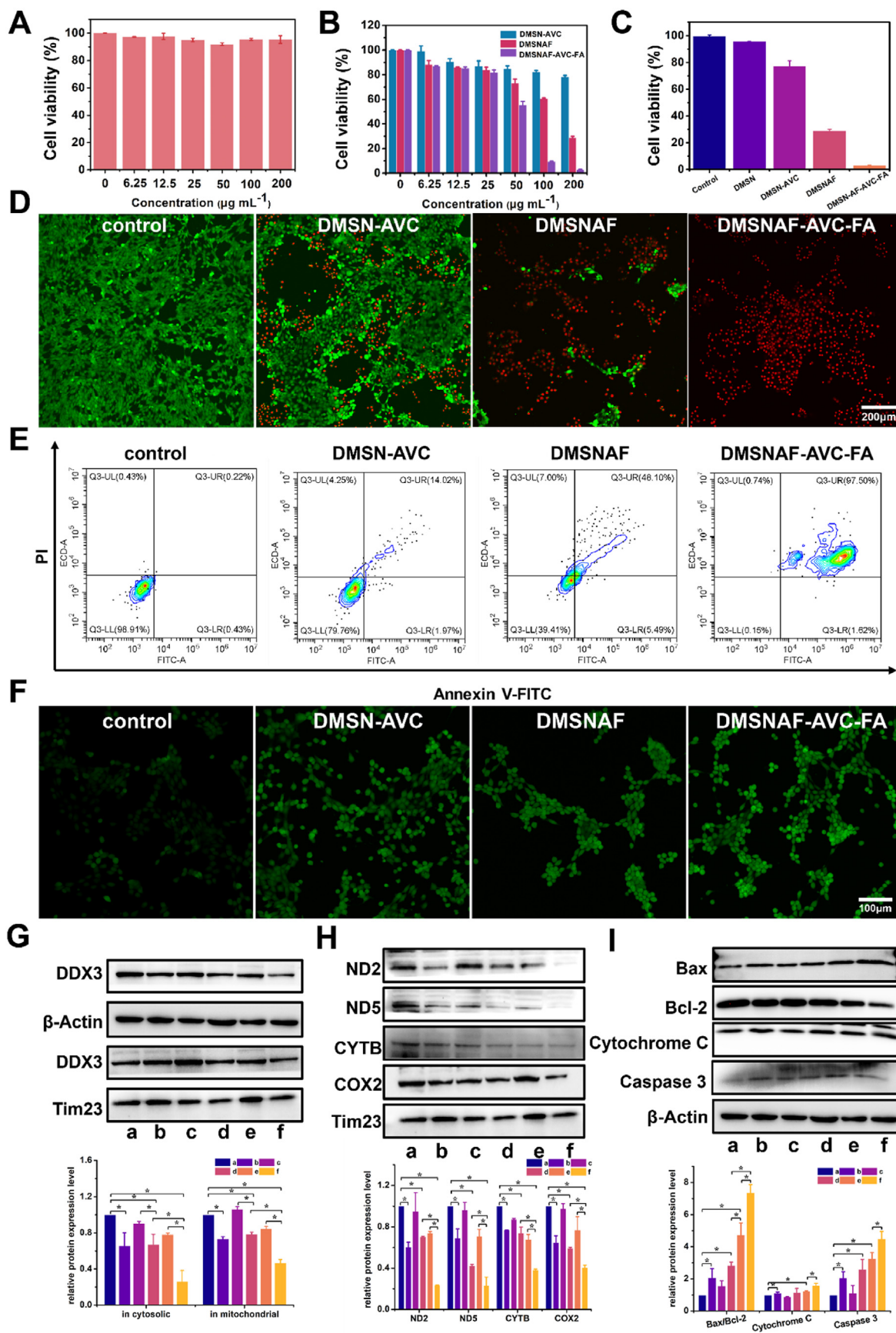
Fig. 3. (A) Cell viability of 4T1 cells after being incubated with AVC and H_2O_2 at varied concentrations. (B) Western blot assay and semiquantitative analysis of DDX3 in cytosolic and mitochondrial. (C) Western blot assay and semiquantitative analysis of ND2, ND5, CYTB, and COX2 in AVC and H_2O_2-treated 4 T cells. (D) Western blot assay and semiquantitative analysis of Cytochrome C, Caspase 3, Bcl-2, Bax and GPx4 in 4T1 cells treated with indicated concentrations of AVC and H_2O_2. Tim23 and β-Actin served as mitochondrial marker and cytosolic marker respectively. (a) PBS, (b) 200 μmol L^{-1} H_2O_2, (c) 400 μmol L^{-1} H_2O_2, (d) 0 μmol L^{-1} H_2O_2+60 μg mL^{-1} AVC, (e) 200 μmol L^{-1} H_2O_2+60 μg mL^{-1} AVC, (f) 400 μmol L^{-1} H_2O_2+60 μg mL^{-1} AVC. Cells treated with PBS were used as a control. (E) The apoptosis pathway of tumor cell triggered by AVC.

catalytic reactions of DMSNAF-AVNC-FA included the self-organized enzymatic cascade reaction by nanozymes and the promoted ROS production by AVC (will discussed later). In the first place, the self-organized enzymatic cascade reaction of DMSNAF-AVC-FA involved two reactions: Au-induced GOx mimicking activity that oxidized glucose into H_2O_2, and the Fe_3O_4-induced POD mimicking activity that further converted as-produced H_2O_2 into •OH via Fenton reaction. As depicted in Fig. 2G, DMSNAF-AVC-FA or glucose alone had a negligible effect on the TMB absorbance, whereas, the one with the addition of both nanozyme and glucose, the absorbance signal at 370 and 652 nm remarkably increased. This proved that DMSNAF-AVC produced the •OH directly without any H_2O_2, and reflected its two-tier GOx and POD mimicking activities of this nanocarrier.

ROS generation capability of DMSNAF-AVC was further validated through electron spin-resonance (ESR) spectrometer. After the addition of 5, 5-dimethyl-1-pyrrolidine-*N*-oxide (DMPO) as spin trap, the DMPO/•OH adduct displayed a typical 1:2:2:1 four-line characteristic spectrum (Supplementary Fig. S8). It was found that the signal of •OH in the mixture of DMSNAF and DMSNAF-AVC was stronger than that DMSN and DMSN-AVC, demonstrating that H_2O_2 produced in Au-catalyzed glucose consumption could efficiently couple with Fe_3O_4 to produce •OH.

3.2. Synergistic antitumor effects for AVC and H_2O_2 co-treatment

Mitochondrion is the primary endogenous source for ROS generation, and the mitochondrial dysfunction is associated with ETC complex I and

(caption on next page)

Fig. 4. (A) Cell viability of L6 cells treated with various concentrations of DMSNAF-AVC-FA for 24 h. (B) Cell viability of 4T1 cells after incubation for 24 h with DMSN-AVC, DMSNAF, or DMSNAF-AVC-FA, at varied concentrations. (C) Cell viability of 4T1 cells with different treatments. (D) Confocal fluorescence images of calcein-AM/PI (E) Apoptosis and necrosis analysis (F) Fluorescence images of DCFH-DA stained 4T1 cells after incubation with fresh medium, DMSN-AVC, DMSNAF, and DMSNAF-AVC-FA. (G) Western blot assay and semiquantitative analysis of DDX3 protein expression performed in cytosolic and mitochondrial with different treatments. (H) Western blot assay and semiquantitative analysis of ND2, ND5, CYTB, and COX2 protein expression with different treatments. (I) Western blot assay and semiquantitative analysis of Cytochrome C, Caspase 3, Bcl-2, and Bax in 4T1 cells with different treatments. Tim23 and β-Actin served as the markers of mitochondrial and cytosolic, respectively. (a) PBS, (b) AVC, (c) DMSN, (d) DMSN-AVC, (e) DMSNAF, (f) DMSNAF-AVC-FA.

III. Disruption of ETC complex results in the leakage of electrons, which can be captured by oxygen to produce ROS [39,40]. Recent studies proved that the high ROS level in cancer cells facilitate AVNs target dead-box RNA helicase 3 (DDX3), and consequently triggering further excessive production of ROS [41–44]. Inspired by these discoveries, we speculate that the elevation of oxidative stress might further promote the pro-oxidant effects of AVC by triggering potent ROS-mediated anti-tumor function via targeting DDX3. To verify this assumption, H_2O_2 (0, 100, 200, 300, 400 μmol L^{-1}) was adopted to induce oxidative stress of tumor cells. Interestingly, AVC treatment resulted in a significant loss of viability in 4T1 cells in both concentration and oxidative stress-dependent manner, i.e., the increase of AVC concentration decreased tumor cell viability, on the other hand, for the AVC treatment with the same concentration, the higher oxidative stress level induced by H_2O_2 displayed a notely lower cell viability (Fig. 3A), such as the groups treated with 90 μg mL^{-1} of AVC, 99% of cell viability without H_2O_2 *vs* 53% of cell viability with 400 μmol L^{-1} of H_2O_2. This confirmed our proposal that the AVC treatment and high oxidative stress indeed have synergistic antitumor efficacy, encouraging us to uncover its underlying mechanism.

As the importance of DDX3 pathway in endogenous ROS production inside the mitochondrial, the pro-oxidant effects of AVC on DDX3 pathway were evaluated. As presented in Fig. 3B, in comparison of group a and group d, the addition of AVC significantly inhibited the protein expression level of DDX3, and down-regulated the protein levels of ND2, ND5 CYTB, and COX2, the subunits of ETC complexes encoded by mitochondrial genes [45] (Fig. 3C). Moreover, as shown in Fig. 3D, the down-regulation of glutathione peroxidase 4 (GPx4) and the up-regulation of the apoptosis-related proteins Bax/Bcl-2, Cytochrome C and cleaved-Caspase-3 suggested that AVC treatment promoted the accumulation of intra-mitochondrial ROS, induced the mitochondrial membrane permeability transition pore (MPTP) open, improved the release of Cytochrome C, and eventually led to tumor cell apoptosis [46]. Overall, these results demonstrate that AVC triggers pro-oxidant effects by the block of mitochondrial translation, damage of ETC complex, and the accumulation of intra-mitochondrial ROS.

To identify the role of elevated oxidative stress in antitumor efficacy, the groups treated with different concentration of H_2O_2 (0, 200, 400 μmol L^{-1}) were also evaluated by western blot analysis. As depicted in Fig. 3B and C, the increased H_2O_2 concentration had negligible effect on the expressions of DDX3 protein in cytoplasm, and a slightly increased DDX3 protein level in mitochondrial, also had no impact on the expression of COX2, ND2, ND5, except a minor downregulation of CYTB. This suggested that the increment of oxidative stress had very limited influences on the ETC complexes, thereby it could not affect the intra-mitochondrial ROS production. However, as shown in Fig. 3D, the increasing oxidative stress levels induced by H_2O_2 significantly promoted the up-regulation of the apoptosis-related proteins Bax/Bcl-2, Cytochrome C and cleaved-Caspase-3, indicating that H_2O_2 treatment also increased the mitochondrial membrane permeability and the release of Cytochrome C, and improved tumor cell apoptosis via activation of Caspase-3 pathway. Based on the above, it suggested that the H_2O_2 treatment induced high oxidative stress level by directly increasing the ROS level in cytoplasm, and the extra-mitochondrial ROS could also damage the mitochondrial membrane permeability, improve the release of Cytochrome C, and activate the cellular apoptosis via Caspase-3 pathway [47].

Taken AVC and H_2O_2 treatments together, the group treated with

400 μmol L^{-1} H_2O_2 and 60 μg mL^{-1} AVC displayed the minimum protein level of DDX3, ND2, ND5 CYTB, COX2, and GPx4, while the maximum protein level of Bax/Bcl-2, Cytochrome C and Caspase-3. These results suggested that the synergistic antitumor efficacy for the co-treatment of AVC and H_2O_2 could elevate the ROS level in both intra- and extra-mitochondrial, thereby synergistically damaging mitochondrial membrane for greater permeability, more released cytochrome C and more activated Caspase-3 pathway, and eventually leading to the boosted tumor cell apoptosis (Fig. 3E).

3.3. Synergistic antitumor effects for DMSNAF-AVC-FA NPs treatment

As shown in Fig. 4A and B, the L6 cells cultivated with various concentrations of DMSNAF-AVC-FA had a great survival rate (95.39%), while for 4T1 cells cultured with the same therapy, the cytotoxicity displayed an appreciable concentration-dependent decrease and achieved an excellent inhibition rate (97%) at 200 μg mL^{-1}. As shown in Supplementary Fig. S9, the green fluorescence of FITC-labeled DMSNAF-AVC-FA after incubation for 2 h located in cytoplasm, confirming the success of endocytosis of these nanoparticles. Similar results of cell viability tests were also observed for H1299 cell line with the apoptosis rate of 82.52% (Supplementary Fig. S10), indicating that the designed therapy was applicable to different tumor types. Altogether, it suggested the designed nanoplatform has excellent biocompatibility, biosafety, and selective cytotoxicity.

Furthermore, as shown in Fig. 4C, DMSNAF-AVC-FA displayed the highest death rate (99.12%) in comparison with DMSN-AVC (15.99%) and DMSNAF (53.49%%), even much higher than the positive control of chemotherapeutic drugs (DOX, Supplementary Fig. S11). Additionally, the effect of FA on cell viability was negligible (Supplementary Fig. S12). Both the calcein-AM (green)/PI (red) co-staining (Fig. 4D) and apoptosis and necrosis analysis (Fig. 4E) further confirmed the synergistic anti-tumor efficacy of DMSNAF-AVC-FA in comparison with either DMSN-AVC or DMSNAF single treatment. The excellent antitumor performance was further proved to be associated to ROS levels, as shown in Fig. 4F that the combination strategy of AVC and DMSNAF produced noticeably stronger green fluorescence and higher ROS level than either individual treatment. As AVC exhibited better pro-oxidative effect under stress milieus, we are encouraged to investigate the mechanism regarding to how DMSNAF-AVC-FA nanoplatform affects ROS, as well as the downstream multiple signaling pathways.

As shown in Fig. 4G, western blot results demonstrated that pure PBS and DMSN cannot affected the DDX3 protein expression, and minor effects of DMSNAF on DDX3 protein expression, while AVC and DMSN-AVC showed a lower level of DDX3 protein expression. The similar trend was also found for the protein expressions of the subunits of ETC complexes (ND2, ND5, CYTB, COX2), as displayed in Fig. 4H. On the other hand, DMSNAF displayed an obvious upregulation of protein levels of Bax, Cytochrome C, and Caspase-3 in comparison of AVC and DMSN-AVC (Fig. 4I). Apparently, treatments of AVC and DMSN-AVC significantly down-regulated the protein expression of DDX3, ND2, ND5, CYTB, COX2, indicating the inhibition of mitochondrial translation and the damage to electron transport pathways that leaded to a high intra-mitochondrial ROS level [29]; in terms of the CDT strategy, DMSNAF showed slight impact on DDX3 and ETC complexes, and consequent minor effects on the intra-mitochondrial ROS production, whereas it significantly promoted the upregulation of Bax/Bcl-2, Cytochrome C, and Caspase-3. This indicated the production of extra-mitochondrial ROS (in
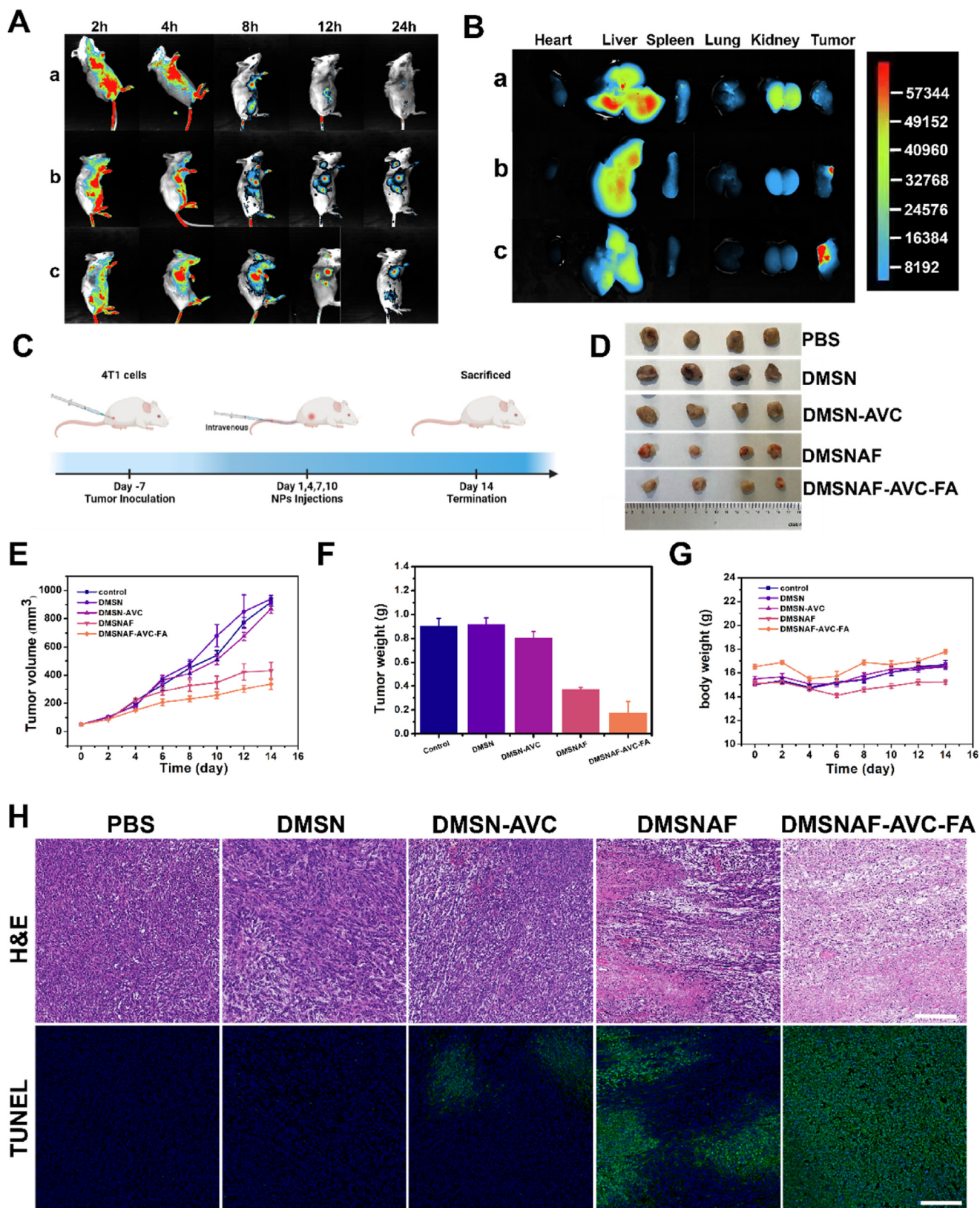
Fig. 5. (A) *In vivo* fluorescent images of 4T1 subcutaneous tumor-bearing mice at various time intervals after i. v. injection of (a) free Cy7, (b) DNSNAF-AVC-Cy7 and (c) DNSNAF-AVC-FA-Cy7. (B) *Ex vivo* fluorescent images of major organs and tumors from 4T1 subcutaneous tumor-bearing mice sacrificed at various time intervals after different treatments. (C) Schematic illustration of *in vivo* therapy for 4T1 subcutaneous tumor-bearing mice. (D) Representative tumor images, (E) tumor volumes, (F) tumor weight, and (G) body weight of 4T1 tumor-bearing nude mice after various treatments for 14 days. (H) H&E and TUNEL staining images of the dissected tumor tissues after 14 days of treatment. Scale bar: 200 μm.

cytoplasm) by CDT also damaged the mitochondrial membrane permeability, and activated the cellular apoptosis via Caspase-3 pathway [48]. Taken AVC and DMSNAF together, DMSNAF-AVC-FA group exhibited the lowest protein level of DDX3, the subunits of ETC complexes (ND2, ND5, CYTB, COX2), and the highest level of Bax/Bcl-2, Cytochrome C, and Caspase-3. These results supported the mechanism for the synergistic antitumor effects of DMSNAF-AVC-FA treatment. DMSNAF treatment that induced ROS production in cytoplasm via Fenton reaction, could damage mitochondrial membrane from outside the mitochondrial and achieve an increased mitochondrial membrane permeability; furthermore, the damaged mitochondrial membrane facilitates AVC migrate into the mitochondrial for greater inhibition of DDX3 pathway and more impaired ETC complexes, which greatly boosted the production of intra-mitochondrial ROS. Under the elevated oxidative stress level via both intra- and extra-mitochondrial ROS, the permeability transition pore (PTP) and the loss of mitochondrial membrane potential (MMP) could be more aggravated, and thereby lead to the maximum release of Cytochrome C and the highest death rate of 4T1 tumor cells via the Caspase 3 pathway.

3.4. In vivo biodistribution and synergistic antitumor effects

Encouraged by the superior anti-tumor capability *in vitro* of DMSNAF-AVC-FA NPs, the *in vivo* antitumor performances were evaluated on the 4T1 tumor-bearing BALB/c mice (Fig. 5). Firstly, the free fluorescent dye Cy7, DMSNAF-AVC-Cy7 and DMSNAF-AVC-FA-Cy7 were intravenously injected into mice to investigate the *in vivo* distribution of the nanocomposites. As shown in Fig. 5A, except for free drug group, the fluorescence emission at the tumor site in the NPs group continuously increased over time and reached the maximum at 24 h post-injection, especially in DMSNAF-AVC-FA-Cy7 group. Furthermore, compared with major organs at 24 h, the solid tumor accommodated a distinctly high content of NPs by observing the ex vivo fluorescence image (Fig. 5B). The fluorescence signals of tumor in the DMSNAF-AVC-FA-Cy7 group were significantly higher than the counterpart group without FA ligand, indicating the excellent target ability of FA liganded NPs [49].

DMSNAF has been widely proven to possess excellent biosafety [33]. Additionally, AVC and FA are both biocompatible ingredients, supplying further evidence for the biosafety of DMSNAF-AVC-FA. Consistent with the *in vitro* experiment groups, 1) PBS, 2) DMSN, 3) DMSN-AVC, 4) DMSNAF, 5) DMSNAF-AVC-FA were chosen for the *in vivo* experiments (Fig. 5C). By analyzing the record of tumor volume and weight, the tumor growth inhibition (TGI) indexes on day 14 were calculated to be 5.2% and 52.9% for the groups of DMSN-AVC and DMSNAF, respectively, indicating their inconspicuous differences in tumor suppression. In contrast, DMSNAF-AVC-FA group displayed the highest TGI index of 63.3% (Fig. 5D–F), remarkably higher than the positive control of chemotherapeutic drugs (DOX (8.4%) and DMSN-DOX (56.7%) (Supplementary Figs. S13–15). In addition, the mice body weight in the treatment groups did not obviously alter during the observation period, revealing a negligible adverse effect on mice metabolism (Fig. 5G, Supplementary Fig. S16). Additionally, hemolysis test (Supplementary Fig. S17) also reflected the biosafety of the NPs even at high concentrations.

Histological observation of tumor sections was conducted by the end of the therapeutic course. No noticeable pathomorphological changes was found from all treatment regimens, suggesting a negligible systemic toxicity. (Supplementary Fig. S18). Hematoxylin and eosin (H&E) staining showed a regular cell structure and intact nucleus morphology in the saline, DMSN and DMSN-AVC groups, while DMSNAF displayed a severe tissue destruction. Distinctly, DMSNAF-AVC-FA underwent the most deleterious tissue damage with the largest nucleus absence. Meanwhile, terminal-deoxynucleotidyl transferase-mediated dUTP nick end-labeling (TUNEL) assay also confirmed the highest apoptotic level caused by DMSNAF-AVC-FA, as verified by the densest green fluorescence dots in the dark field (Fig. 5H). In terms of the positive control, the

chemotherapeutic drugs only induced a minor degree of tissue damage and apoptosis (Supplementary Fig. S19). All these findings demonstrated DMSN-AVC-FA exhibited an excellent antitumor efficacy *in vivo*, especially the obvious synergistic effects upon either AVC or DMSNAF individual treatment.

4. Conclusion

In summary, inspired by the pro-apoptosis effects and selective cytotoxicity of polyphenols on tumor cells, we have designed and constructed a nanozyme-based polyphenol/CDT combined strategy to boost ROS generation. For the first time, the DMSNAF-AVC-FA nanoplatform exerts a typical CDT effect of ROS production mediated by Au and Fe_3O_4, which damages the mitochondrial membrane, releasing Cytochrome C, and leads to cell apoptosis; on the other hand, the improved mitochondrial membrane permeability also facilitates AVC migrate into mitochondrial, targeting the DDX3 pathway and impairing the ETC complexes, thus significantly boosting the endogenous ROS levels inside the mitochondrial. Both extra-mitochondrial ROS production by CDT and intra-mitochondrial ROS promotion by AVC significantly boosts the release of Cytochrome C and causes the maximum tumor cell apoptosis via Caspase-3 pathway. Overall, the designed system exhibits excellent antitumor performance both *in vitro* and *in vivo*, with minimum toxicity on normal cells. This bioinspired strategy provides new insight into the clinical conversion of CDT treatment. In the future, more efforts could be focused on biological effects and biosafety *in vivo* for a better clinical conversion of CDT/polyphenol combined therapy.

Authorship contribution statement

Huijia Mao: Data curation, Experiment conduction, paper draft review and revision; **Yangyang Wen**: Methodology, Resources; paper draft review and revision; **Yonghui Yu**: Experiment conduction, Methodology; **Hongyan Li**: Supervision, Project administration, paper draft review and revision; **Jing Wang**: Supervision, Editing, Revision; **Baoguo Sun**: Supervision, Funding acquisition, Paper editing, Revision

Declaration of competing interest

The authors declare that they have no known competing financial interests or personal relationships that could have appeared to influence the work reported in this paper.

Data availability

Data will be made available on request.

Acknowledgements

Appendix A. Supplementary data

Supplementary data to this article can be found online at https://doi.org/10.1016/j.mtbio.2022.100436.

References

[1] S. Li, P. Jiang, F. Jiang, Y. Liu, Recent advances in nanomaterial-based nanoplatforms for chemodynamic cancer therapy, Adv. Funct. Mater. 31 (2021), 2100243, https://doi.org/10.1002/adfm.202100243.

[2] S. Goel, C.A. Ferreira, F. Chen, P.A. Ellison, C.M. Siamof, T.E. Barnhart, W.B. Cai, Activatable hybrid nanotheranostics for tetramodal imaging and synergistic photothermal/photodynamic therapy, Adv. Mater. 30 (2018), 1704367, https://doi.org/10.1002/adma.201704367.

[3] Y. Wang, J. Chen, R. Duan, R. Gu, W. Wang, J. Wu, H. Lian, Y. Hu, A. Yuan, High-Z-sensitized radiotherapy synergizes with the intervention of the pentose phosphate pathway for in situ tumor vaccination, Adv. Mater. 34 (2022), 2109726, https://doi.org/10.1002/adma.202109726.

[4] J. Nam, S. Son, K.S. Park, W.P. Zou, L.D. Shea, J.J. Moon, Cancer nanomedicine for combination cancer immunotherapy, Nat. Rev. Mater. 4 (2019) 398–414, https://doi.org/10.1038/s41578-019-0108-1.

[5] D. Salas-Benito, J.L. Perez-Gracia, M. Ponz-Sarvise, M.E. Rodriguez-Ruiz, I. Martinez-Forero, E. Castanon, J.M. Lopez-Picazo, M.F. Sanmamed, I. Melero, Paradigms on immunotherapy combinations with chemotherapy, Cancer Discov. 11 (2021) 1353–1367, https://doi.org/10.1158/2159-8290.Cd-20-1312.

[6] Z. Yang, Y. Luo, Y. Hu, K. Liang, G. He, Q. Chen, Q. Wang, H. Chen, Photothermo-promoted nanocatalysis combined with H2S-mediated respiration inhibition for efficient cancer therapy, Adv. Funct. Mater. 31 (2021), 2007991, https://doi.org/10.1002/adfm.202007991.

[7] K. Liang, Z. Li, Y. Luo, Q. Zhang, F. Yin, L. Xu, H. Chen, H. Wang, Intelligent nanocomposites with intrinsic blood-brain-barrier crossing ability designed for highly specific MR imaging and sonodynamic therapy of glioblastoma, Small 16 (2020), 1906985, https://doi.org/10.1002/smll.201906985.

[8] Y. Zhuang, S. Han, Y. Fang, H. Huang, J. Wu, Multidimensional transitional metal-actuated nanoplatforms for cancer chemodynamic modulation, Coord. Chem. Rev. 455 (2022), 214360, https://doi.org/10.1016/j.ccr.2021.214360.

[9] B. Yang, J. Shi, Ascorbate tumor chemotherapy by an iron-engineered nanomedicine-catalyzed tumor-specific pro-oxidation, J. Am. Chem. Soc. 142 (2020) 21775–21785, https://doi.org/10.1021/jacs.0c09984.

[10] Z. Tang, P. Zhao, H. Wang, Y. Liu, W. Bu, Biomedicine meets Fenton chemistry, Chem. Rev. 121 (2021) 1981–2019, https://doi.org/10.1021/acs.chemrev.0c00977.

[11] X. Li, H. Sun, H. Li, C. Hu, Y. Luo, X. Shi, A. Pich, Multi-responsive biodegradable cationic nanogels for highly efficient treatment of tumors, Adv. Funct. Mater. 31 (2021), 2100227, https://doi.org/10.1002/adfm.202100227.

[12] H. Sun, T. Yu, X. Li, Y. Lei, J. Li, X. Wang, P. Peng, D. Ni, X. Wang, Y. Luo, Second near-infrared photothermal-amplified immunotherapy using photoactivatable composite nanostimulators, J. Nanobiotechnol. 19 (2021) 1–17, https://doi.org/10.1186/s12951-021-01197-5.

[13] Z. Tang, Y. Liu, M. He, W. Bu, Chemodynamic therapy: tumour microenvironment-mediated Fenton and fenton-like reactions, Angew. Chem. Int. Ed. 58 (2019) 946–956, https://doi.org/10.1002/anie.201805664.

[14] M.S. Ricci, W. Zong, Chemotherapeutic approaches for targeting cell death pathways, Oncol. 11 (2006) 342–357, https://doi.org/10.1634/theoncologist.11-4-342.

[15] W. Fernando, H.P.V. Rupasinghe, D.W. Hoskin, Dietary phytochemicals with anti-oxidant and pro-oxidant activities: a double-edged sword in relation to adjuvant chemotherapy and radiotherapy? Cancer Lett. 452 (2019) 168–177, https://doi.org/10.1016/j.canlet.2019.03.022.

[16] M. Lopez-Lazaro, Dual role of hydrogen peroxide in cancer: possible relevance to cancer chemoprevention and therapy, Cancer Lett. 252 (2007) 1–8, https://doi.org/10.1016/j.canlet.2006.10.029.

[17] T. Xue, C. Xu, Y. Wang, Y. Wang, H. Tian, Y. Zhang, Doxorubicin-loaded nanoscale metal-organic framework for tumor-targeting combined chemotherapy and chemodynamic therapy, Biomater. Sci. 7 (2019) 4615–4623, https://doi.org/10.1039/c9bm01044k.

[18] Y. Xu, Y. Guo, C. Zhang, M. Zhan, L. Jia, S. Song, C. Jiang, M. Shen, X. Shi, Fibronectin-coated metal-phenolic networks for cooperative tumor chemo-/chemodynamic/immune therapy via enhanced ferroptosis-mediated immunogenic cell death, ACS Nano 16 (2022) 984–996, https://doi.org/10.1021/acsnano.1c08585.

[19] B. Ding, S. Shao, F. Jiang, P. Dang, C. Sun, S. Huang, P. Ma, D. Jin, A.A. Al Kheraif, J. Lin, MnO2-Disguised upconversion hybrid nanocomposite: an ideal architecture for tumor microenvironment-triggered UCL/MR bioimaging and enhanced chemodynamic therapy, Chem. Mater. 31 (2019) 2651–2660, https://doi.org/10.1021/acs.chemmater.9b00893.

[20] W. Wu, Y. Pu, J. Shi, Nanomedicine-enabled chemotherapy-based synergetic cancer treatments, J. Nanobiotechnol. 20 (2022) 4, https://doi.org/10.1186/s12951-021-01181-z.

[21] Y. Liang, Z. Liu, P. Wang, Y. Li, R. Wang, S. Xie, Nanoplatform-based natural products co-delivery system to surmount cancer multidrug-resistant, J. Contr. Release 336 (2021) 396–409, https://doi.org/10.1016/j.jconrel.2021.06.034.

[22] S. NavaneethaKrishnan, J.L. Rosales, K.Y. Lee, ROS-mediated cancer cell killing through dietary phytochemicals, Oxid. Med. Cell. Longev. 2019 (2019), 9051542, https://doi.org/10.1155/2019/9051542.

[23] A.J. Leon-Gonzalez, C. Auger, V.B. Schini-Kerth, Pro-oxidant activity of polyphenols and its implication on cancer chemoprevention and chemotherapy, Biochemist 98 (2015) 371–380, https://doi.org/10.1016/j.bcp.2015.07.017.

[24] Y. Bi, C. Shen, C. Li, Y. Liu, D. Gao, C. Shi, F. Peng, Z. Liu, B. Zhao, Z. Zheng, X. Wang, X. Hou, H. Liu, J. Wu, H. Zou, K. Wang, C. Zhong, J. Zhang, C. Shi, S. Zhao, Inhibition of autophagy induced by quercetin at a late stage enhances cytotoxic effects on glioma cells, Tumor Biol. 37 (2016) 3549–3560, https://doi.org/10.1007/s13277-015-4125-4.

[25] Q. Zhang, G. Cheng, H. Qiu, L. Zhu, Z. Ren, W. Zhao, T. Zhang, L. Liu, The p53-inducible gene 3 involved in flavonoid-induced cytotoxicity through the reactive oxygen species-mediated mitochondrial apoptotic pathway in human hepatoma cells, Food Funct. 6 (2015) 1518–1525, https://doi.org/10.1039/c5fo00142k.

[26] Q. Chen, M.G. Espey, A.Y. Sun, C. Pooput, K.L. Kirk, M.C. Krishna, D.S. Khosh, J. Drisko, M. Levine, Pharmacologic doses of ascorbate act as a prooxidant and decrease growth of aggressive tumor xenografts in mice, Natl. Acad. Sci. U.S.A. 105 (2008) 11105–11109, https://doi.org/10.1073/pnas.0804226105.

[27] M. Lopez-Lazaro, J.M. Calderon-Montano, E. Burgos-Moron, C.A. Austin, Green tea constituents (-)-epigallocatechin-3-gallate (EGCG) and gallic acid induce topoisomerase I- and topoisomerase II-DNA complexes in cells mediated by pyrogallol-induced hydrogen peroxide, Mutagenesis 26 (2011) 489–498, https://doi.org/10.1093/mutage/ger006.

[28] T.P. Szatrowski, C.F. Nathan, Production of large amounts of hydrogen peroxide by human tumor cells, Cancer Res. 51 (1991) 794–798.

[29] R. Fu, P. Yang, Z. Li, W. Liu, S. Amin, Z. Li, Avenanthramide A triggers potent ROS-mediated anti-tumor effects in colorectal cancer by directly targeting DDX3, Cell Death Dis. 10 (2019) 593, https://doi.org/10.1038/s41419-019-1825-5.

[30] Z. Zhang, L. Xie, Y. Ju, Y. Dai, Recent advances in metal-phenolic networks for cancer theranostics, Small 17 (2021), 2100314, https://doi.org/10.1002/smll.202100314.

[31] X. Chen, R. Ma, Z. Fu, Q. Su, X. Luo, Y. Han, Y. Yang, Q. Deng, Metal-phenolic networks-encapsulated cascade amplification delivery nanoparticles overcoming cancer drug resistance via combined starvation/chemodynamic/chemo therapy, Chem. Eng. J. 442 (2022), https://doi.org/10.1016/j.cej.2022.136221.

[32] J.H. Han, J. Shin, J. Lee, J.M. Kang, J.H. Park, C.G. Park, D.K. Han, I.H. Kim, W. Park, Combination of metal-phenolic network-based immunoactive nanoparticles and bipolar irreversible electroporation for effective cancer immunotherapy, Small 18 (2022), https://doi.org/10.1002/smll.202200316.

[33] S. Gao, H. Lin, H. Zhang, H. Yao, Y. Chen, J. Shi, Nanocatalytic tumor therapy by biomimetic dual inorganic nanozyme-catalyzed cascade reaction, Adv. Sci. 6 (2019), 1801733, https://doi.org/10.1002/advs.201801733.

[34] Y. Niu, Y. Yang, Z. Yang, X. Wang, P. Zhang, L. Lv, Y. Liu, Y. Liu, Y. Zhou, Aptamer-immobilized bone-targeting nanoparticles in situ reduce sclerostin for osteoporosis treatment, Nano Today 45 (2022), 101529, https://doi.org/10.1016/j.nantod.2022.101529.

[35] B. Yang, H. Yao, H. Tian, Z. Yu, Y. Guo, Y. Wang, J. Yang, C. Chen, J. Shi, Intratumoral synthesis of nano-metalchelate for tumor catalytic therapy by ligand field-enhanced coordination, Nat. Commun. 12 (2021), https://doi.org/10.1038/s41467-021-23710-y.

[36] B. Yang, Y. Guo, Y. Wang, J. Yang, H. Yao, J. Shi, Nanomedicine-leveraged intratumoral coordination and redox reactions of dopamine for tumor-specific chemotherapy, Ccs Chemistry 4 (2022) 1499–1509, https://doi.org/10.31635/ccschem.021.202100930.

[37] Y. Sang, F. Cao, W. Li, L. Zhang, Y. You, Q. Deng, K. Dong, J. Ren, X. Qu, Bioinspired construction of a nanozyme-based H2O2 homeostasis disruptor for intensive chemodynamic therapy, J. Am. Chem. Soc. 142 (2020) 5177–5183, https://doi.org/10.1021/jacs.9b12873.

[38] M. Huo, L. Wang, Y. Chen, J. Shi, Tumor-selective catalytic nanomedicine by nanocatalyst delivery, Nat. Commun. 8 (2017) 357, https://doi.org/10.1038/s41467-017-00424-8.

[39] Y. Chen, J.L. Zweier, Cardiac mitochondria and reactive oxygen species generation, Circ. Res. 114 (2014) 524–537, https://doi.org/10.1161/circresaha.114.300559.

[40] J. Xu, L. Ji, Y. Ruan, Z. Wan, Z. Lin, S. Xia, L. Tao, J. Zheng, L. Cai, Y. Wang, X. Liang, X. Cai, UBQLN1 mediates sorafenib resistance through regulating mitochondrial biogenesis and ROS homeostasis by targeting PGC1 beta in hepatocellular carcinoma, Signal Transduct. Targeted Ther. 6 (2021) 190, https://doi.org/10.1038/s41392-021-00594-4.

[41] O. Shriwas, M. Priyadarshini, S.K. Samal, R. Rath, S. Panda, S.K. Das Majumdar, D.K. Muduly, R. Botlagunta, R. Dash, DDX3 modulates cisplatin resistance in OSCC through ALKBH5-mediated m(6)A-demethylation of FOXM1 and NANOG, Apoptosis 25 (2020) 233–246, https://doi.org/10.1007/s10495-020-01591-8.

[42] S.K. Samal, S. Routray, G.K. Veeramachaneni, R. Dash, M. Botlagunta, Ketorolac salt is a newly discovered DDX3 inhibitor to treat oral cancer, Sci. Rep. 5 (2015) 9982, https://doi.org/10.1038/srep09982.

[43] G.M. Bol, F. Vesuna, M. Xie, J. Zeng, K. Aziz, N. Gandhi, A. Levine, A. Irving, D. Korz, S. Tantravedi, M.R.H. Van Voss, K. Gabrielson, E.A. Bordt, B.M. Polster, L. Cope, P. van der Groep, A. Kondaskar, M.A. Rudek, R.S. Hosmane, E. van der Wall, P.J. van Diest, P.T. Tran, V. Raman, Targeting DDX3 with a small molecule inhibitor for lung cancer therapy, EMBO Mol. Med. 7 (2015) 648–669, https://doi.org/10.15252/emmm.201404368.

[44] M. Botlagunta, B. Kollapalli, L. Kakarla, S. Gajarla, S.P. Gade, C.L. Dadi, A. Penumadu, S. Javeed, In vitro anti-cancer activity of doxorubicin against human RNA helicase, DDX3, Bioinformatics 12 (2016) 347–353, https://doi.org/10.6026/97320630012347.

[45] A. Erdem, S. Marin, D.A. Pereira-Martins, M. Geugien, A. Cunningham, M.G. Pruis, I. Weinhauser, A. Gerding, B.M. Bakker, A.T.J. Wierenga, E.M. Rego, G. Huls, M. Cascante, J.J. Schuringa, Inhibition of the succinyl dehydrogenase complex in acute myeloid leukemia leads to a lactate-fuelled respiratory metabolic vulnerability, Nat. Commun. 13 (2022) 2013, https://doi.org/10.1038/s41467-022-29639-0.

[46] S. Zhang, L. Jin, J. Liu, Y. Wang, T. Zhang, Y. Liu, Y. Zhao, N. Yin, R. Niu, D. Xue, Y. Yu, Y. Yang, Novel FeF2/Fe1-xS nanoreactor-mediated mitochondrial dysfunction via oxidative stress and fluoride ions overloaded for synergistic chemodynamic therapy and photothermal therapy, Adv. Funct. Mater. 32 (2022), 2113397, https://doi.org/10.1002/adfm.202113397.

[47] W. Bao, M. Liu, J. Meng, S. Liu, S. Wang, R. Jia, Y. Wang, G. Ma, W. Wei, Z. Tian, MOFs-based nanoagent enables dual mitochondrial damage in synergistic

antitumor therapy via oxidative stress and calcium overload, Nat. Commun. 12 (2021) 6399, https://doi.org/10.1038/s41467-021-26655-4.

[48] X. Yang, X. Xu, M. Wang, H. Xu, X. Peng, N. Han, T. Yu, L. Li, Q. Li, X. Chen, Y. Wen, T. Li, A nanoreactor boosts chemodynamic therapy and ferroptosis for synergistic cancer therapy using molecular amplifier dihydroartemisinin, J. Nanobiotechnol. 20 (2022) 230, https://doi.org/10.1186/s12951-022-01455-0.

[49] W. Poon, B.R. Kingston, B. Ouyang, W. Ngo, W.C.W. Chan, A framework for designing delivery systems, Nat. Nanotechnol. 15 (2020) 819–829, https://doi.org/10.1038/s41565-020-0759-5.